Available online at www.sciencedirect.com

ScienceDirect

Ceramics International 39 (2013) 9331–9341

CERAMICS INTERNATIONAL

www.elsevier.com/locate/ceramint

Properties and microstructural analysis of $La_{1-x}Sr_xGa_{1-y}Mg_yO_{3-\delta}$ solid electrolyte ceramic

Yu-Chuan Wu*, Ming-Ze Lee

Department of Materials and Mineral Resources Engineering, National Taipei University of Technology, Taipei 10608, Taiwan, ROC

Received 13 April 2013; received in revised form 12 May 2013; accepted 13 May 2013
Available online 23 May 2013

Abstract

$La_{1-x}Sr_xGa_{1-y}Mg_yO_{3-\delta}$ ($x=0.1$–0.2, $y=0.1$–0.2) (LSGM) electrolytes, which have high ionic conductivities, were synthesized by a solid-state reaction at 1500 °C. In our study, $La_{0.9}Sr_{0.1}Ga_{0.9}Mg_{0.1}O_{3-\delta}$ and $La_{0.9}Sr_{0.1}Ga_{0.8}Mg_{0.2}O_{3-\delta}$ crystallized in an orthorhombic (*Imma*) structure, and $La_{1-x}Sr_xGa_{1-y}Mg_yO_{3-\delta}$ ($0.1 < x \leq 0.2$, $0.17 \leq y \leq 0.2$) crystallized in a rhombohedral ($R\bar{3}c$) structure. Active Raman bands at approximately 532, 674, and 750 cm^{-1} were observed in these samples because of the decrease in local symmetry induced by the oxygen vacancies. When $x+y > 0.35$, the conductivity was approximately 0.164–0.173 S/cm at 800 °C. The ionic conductivity mechanism changed at temperatures of approximately 500–650 °C. $La_{0.9}Sr_{0.1}Ga_{0.9}Mg_{0.1}O_{3-\delta}$ and $La_{0.9}Sr_{0.1}Ga_{0.8}Mg_{0.2}O_{3-\delta}$ samples possessed higher resistances at 300–400 °C as a result of existing stacking faults and defects. The thermal expansion coefficients (TECs) were approximately 9.1×10^{-6}/°C to 11×10^{-6}/°C at 200–500 °C.

Keywords: A. Sintering; B. Electron microscopy; C. Ionic conductivity; E. Fuel cell

1. Introduction

Solid-oxide fuel cells (SOFCs) have been studied over the past few decades. SOFCs that operate at lower operating temperatures (600–800 °C) are called intermediate-temperature SOFCs. Among solid electrolytes, $La_{1-x}Sr_xGa_{1-y}Mg_yO_{3-\delta}$ electrolytes are good, purely ionic conductors (> 0.1 S/cm at 800 °C) with high chemical stability at oxygen partial pressures of approximately 10^{-22} to 1 atm and stable performances over long operating times [1,2].

$LaGaO_3$ undergoes a structural phase transition from an orthorhombic (*Pbnm*) to a rhombohedral ($R\bar{3}c$) structure at 145 °C and further transforms to a cubic ($Pm\bar{3}m$) structure at 1000 °C [3–5]. However, previous reports [5–8] showed that Sr- and Mg-doped lanthanum gallates have five crystal structures from room temperature to high temperature: two orthorhombic (*Pnma*, denoted as PO, and *Imma*, denoted as IO), monoclinic (*I2/a*, denoted as M), rhombohedral ($R\bar{3}c$, denoted as hR), and cubic ($Pm\bar{3}m$, denoted as C). Guenter et al. [7] also reported that the crystal structures of $La_{0.9}Sr_{0.1}Ga_{0.9}Mg_{0.1}O_{3-\delta}$ and $La_{0.9}Sr_{0.1}Ga_{0.8}Mg_{0.2}O_{3-\delta}$ are orthorhombic (*Imma)* at room temperature.

Oxygen vacancies are created by doping with divalent ions, replacing the La and Ga atoms, which improves the ionic conductivity [9]. The best divalent ions are Sr and Mg; however, secondary phases, e.g., $LaSrGa_3O_7$, $LaSrGaO_4$, and $La_4Ga_2O_9$, are easily produced from LSGM systems and lead to a lower conductivity [9,10]. The changes in the slope of the Arrhenius plot coincide with structural transitions and changes in the thermal expansion coefficient (TEC) [6]. In air, the oxygen transference numbers vary from 0.984 to 0.998 and decrease with increasing temperature or oxygen partial pressure (P_{O_2}) [11,12]. At low temperatures, the oxygen vacancies (denoted as $V_{\ddot{O}}$) in the LSGM oxygen sublattice are in the GaO_5-$V_{\ddot{O}}$-GaO_5 state, resulting in a higher activation energy ($E_a \approx 1$ eV). At temperatures above 500 °C, the vacancies are in the $Ga(O_{5/6}V_{O1/6})_6$ state, and E_a is approximately 0.7 eV [4]. The $La_{0.8}Sr_{0.2}Ga_{0.83}Mg_{0.17}O_{3-\delta}$ sample had a higher ionic conductivity of 0.17 S/cm at 800 °C [2]. Mg doping at the B-site had a stronger effect on the TEC than did

*Corresponding author. Postal address: 1, Sec. 3, Chung-hsiao E. Rd., Taipei 10608, Taiwan, ROC. Tel.: +886 2 27712171x2765; fax: +886 2 27317185.
E-mail addresses: wuyc@ntut.edu.tw, wuyc@mail.ntut.edu.tw (Y.-C. Wu).

0272-8842/$ - see front matter © 2013 Elsevier Ltd and Techna Group S.r.l. All rights reserved.
http://dx.doi.org/10.1016/j.ceramint.2013.05.050

Sr doping at the A-site; the TEC of the $La_{0.8}Sr_{0.2}Ga_{0.8}Mg_{0.2}O_{3-\delta}$ sample was approximately 10.47×10^{-6}/°C [13,14].

In the present work, the microstructures and electrical properties of $La_{1-x}Sr_xGa_{1-y}Mg_yO_{3-\delta}$ were measured by X-ray diffractometry (XRD), Raman spectroscopy, scanning electron microscopy (SEM), transmission electron microscopy (TEM), and frequency response analysis. The purpose of this work is to determine the relationship between the electrical properties and microstructural changes of the various compounds.

2. Experimental procedure

2.1. Preparation of LSGM samples

La_2O_3 (99.99%, Showa Denko, Kanagawa, Japan), $SrCO_3$ (99.9%, Showa Denko, Kanagawa, Japan), Ga_2O_3 (99.99%, D.F. Goldsmith, Illinois, USA), and MgO (99.9%, J.T. Baker, Pennsylvania, USA) powders were mixed to form the $La_{1-x}Sr_xGa_{1-y}Mg_yO_{3-\delta}$ samples by solid-state reaction, and the La_2O_3 powder was first fired at 1200 °C for 5 h. The $La_{1-x}Sr_xGa_{1-y}Mg_yO_{3-\delta}$ specimens are designated as LSGM*AB*, where *A* and *B* indicate the Sr and Mg contents in mol% respectively. The compound powders were ball milled in ethanol for 24 h, and then the slurries were dried. The dried powders were deagglomerated using an agate mortar and pestle and then calcined at 1250 °C for 5 h (heating rate 5 °C/min). The calcined powders were ball milled again to reduce the size of the agglomerated powder and improve the sintered densification. The powders were dried and deagglomerated again using an agate mortar and pestle and then passed through a 200-mesh sieve. Finally, the powders were pressed into disks by uniaxial pressing under a pressure of 150 MPa. These pellets were burned out at 550 °C for 4 h and then sintered at 1550 °C for 10 and 15 h at a heating rate of 5 °C/min. The relative densities were estimated using the Archimedes method.

2.2. Crystal structure and microstructural analysis

First, the surfaces of the sintered samples were polished and coated with a thin Au film. The samples were then heat treated at 450 °C. The diffraction peak (2θ=38.18°) of the Au film was used as the internal standard peak for XRD analysis. The crystal structure was identified by X-ray diffractometry (XRD, Rigaku DMX2200, Tokyo, Japan) with Cu Kα radiation, operated at 40 kV and 30 mA, and also analyzed at room temperature by Raman spectroscopy (Labram HR800 UV, Horiba Jobin Yvon, France).

The polished samples were chemically etched, and the microstructures were analyzed by scanning electron microscopy (SEM, Hitachi S-4700, Tokyo, Japan) at 15 kV and 10 mA. The bright field images and selected area electron diffraction (SAED) patterns were obtained by transmission electron microscopy (TEM, JEOL™ 2100F, Tokyo, Japan).

2.3. Analysis of physical and electrical properties

The TECs of the samples were measured in air using a NETZSCH 402C dilatometer (NETZSCH, Germany) in the temperature range of 50–800 °C at a heating rate of 5 °C/min.

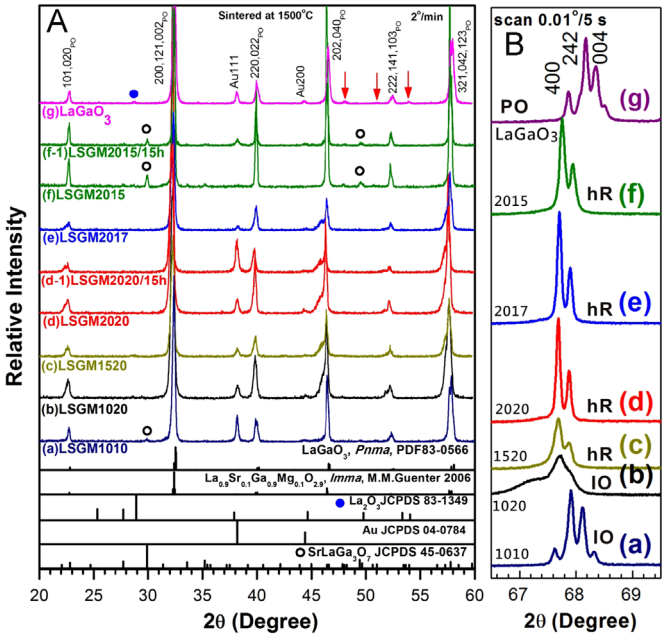

Fig. 1. (a) LSGM1010, (b) LSGM1020, (c) LSGM1520, (d) LSGM2020, (e) LSGM2017, (f) LSGM2015, and (g) $LaGaO_3$ samples sintered at 1500 °C for 10 h and (d-1) and (f-1) the corresponding samples sintered at 1500 °C for 15 h. The scanning conditions of XRD are 2deg/min in (A) and 0.01deg/5 s in (B).

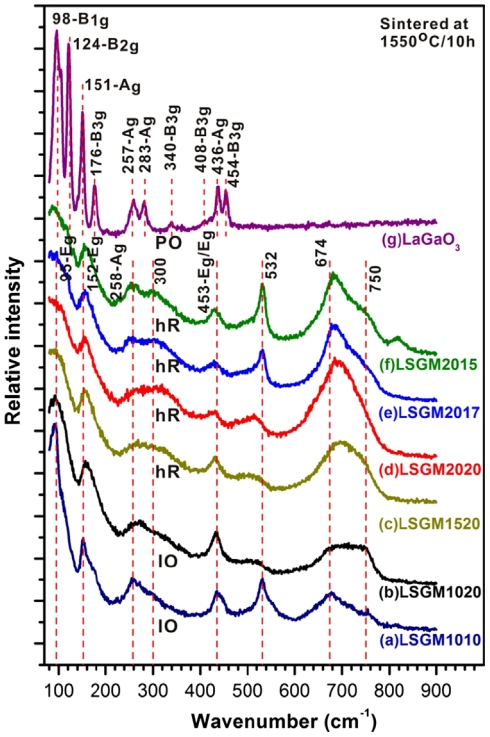

Fig. 2. Raman spectra of the LSGM specimens at room temperature.

The dilatometer was calibrated using the NETZSCH Al_2O_3 standard. Pellets with diameters of 1 cm were wet-ground to a thickness of approximately 1 mm. Electrodes were formed by screen-printing silver (Ag) paste onto both sides of the samples, creating a Ag area of $5 \times 5\ mm^2$ and then fired at 800 °C in air. AC impedance spectra were measured with a frequency response analyzer (HIOKI-3532-50, USA) over a frequency range from 42 Hz to 5×10^6 Hz with an AC voltage of 1 V in air, and the operating temperature was increased from 300 °C to 800 °C in intervals of 100 °C. Ag wires were used as current collectors. Each measurement was allowed to reach equilibrium prior to recording the data. The impedance spectra were fitted with equivalent circuits. The conductivities of the samples were also measured using the dc four-point probe method in air at an applied voltage of 10 V as the operating temperature was increased from 500 °C to 800 °C in intervals of 50 °C.

3. Results and discussion

3.1. Structural analysis

Fig. 1(A) shows the XRD patterns of the $La_{1-x}Sr_xGa_{1-y}Mg_yO_{3-\delta}$ (x=0–0.2, y=0–0.2) samples sintered at 1500 °C for 10 and 15 h. Three additional peaks (2θ=48°, 51.2°, and 53.9°) appeared in the $LaGaO_3$ sample [Fig. 1(A)(g)], indicating an orthorhombic (*Pnma*) phase (JCPDS 83-0566); this sample also contained fewer La_2O_3 (JCPDS 83-1349) impurities (2θ=29°). Fig. 1(B) shows the XRD patterns resulting from slow scanning at 2θ=66.5–69.5°, and the LSGM1010 and LSGM1020 samples exhibit an orthorhombic (*Imma*) phase. Fig. 1(A)(c)–(f) and (B)(c)–(f) shows that the structures of these specimens had changed and no longer contained an orthorhombic (*Pnma*) phase; rather, they featured a rhombohedral ($R\bar{3}c$) phase, as observed at 2θ=67–69°.

According to a report by Guenter et al. [7], the crystal structure of $La_{0.9}Sr_{0.1}Ga_{0.9}Mg_{0.1}O_{3-\delta}$ is orthorhombic *Imma* at room temperature, which is similar to the results of our study. A $SrLaGa_3O_7$ phase (JCPDS 45-0637) was also detected at 2θ=29.9° in the LSGM1010 and LSGM2015 samples [Fig. 1(A)]; however, $SrLaGa_3O_7$ is an insulator and will therefore lower the overall conductivity. Consequently, doping with Sr and Mg ions, which have larger ionic radii, can decrease the tilting angle of the octahedral GaO_6, thereby slightly increasing the structural symmetry, as shown in Fig. 1(B)(c)–(f). As the sintering time increased from 10 to 15 h, the crystal structure did not change [Fig. 1(A)]. However, the asymmetric peaks at 2θ=46° in Fig. 1(A)(b)–(e) cannot be assigned to the orthorhombic structure, and their source is not clear.

3.2. Raman spectra

Fig. 2 shows the Raman spectra of LSGM samples at room temperature. According to the report of Tompsett et al. [15], the 17 bands of PO-$LaGaO_3$ and 4 bands of hR-$LaGaO_3$ were observed at 21 °C and 500 °C, respectively, in the Raman spectra. Fig. 2(g) shows that the $LaGaO_3$ sample has a PO-structure, and bands are observed in the range 50–900 cm^{-1}:

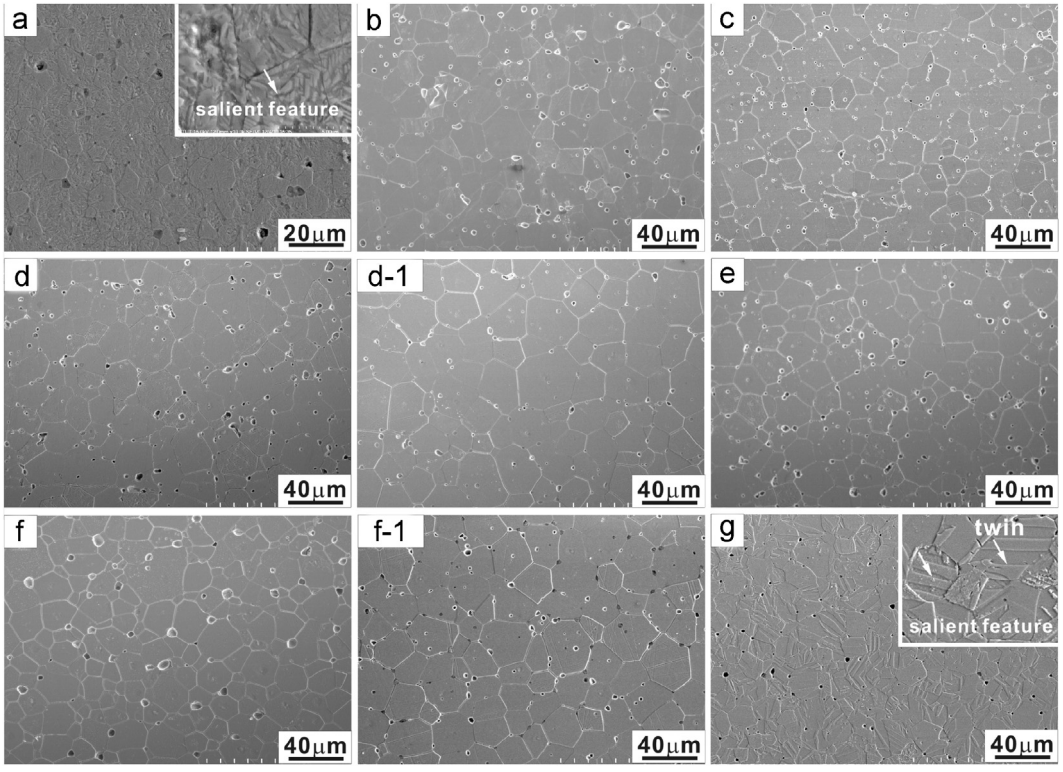

Fig. 3. SEM images of the LSGM samples sintered at 1500 °C for 10 or 15 h, (a) LSGM1010, (b) LSGM1020, (c) LSGM1520, (d) LSGM2020, (d-1) LSGM2020 (15 h), (e) LSGM2017, (f) LSGM2015, (f-1) LSGM2015 (15 h), and (g) $LaGaO_3$ (chemically etched).

98(B_{1g}), 124(B_{2g}), 151(A_g), 176(B_{3g}), 257(A_g), 283(A_g), 340(B_{3g}), 408(B_{3g}), 436(A_g), and 454(B_{3g}) cm^{-1}. The Raman spectra of the LSGM samples are different from that of the $LaGaO_3$ sample, which indicate that the structures have changed [as shown in Fig. 2(a)–(f)]. The Raman peaks in Fig. 2(c)–(f) are broader than those of LSGM1010 and LSGM1020, as shown in Fig. 2(a) and (b) and, according to the XRD analysis in Fig. 1 (B), correspond to hR- and IO-structures, respectively.

Three active bands at approximately 532, 674, and 750 cm^{-1} appear in the range 470–900 cm^{-1} in Fig. 2(a)–(f), and their scattering intensity depends on the amount of Sr and Mg. These three active bands arise from the decrease in local symmetry induced by the oxygen vacancies [16], as shown in the following:

$$MgO + SrO \xrightarrow{LaGaO_3} Mg'_{Ga} + Sr'_{La} + V_O^{\cdot\cdot} + 2O_O^X \quad (1)$$

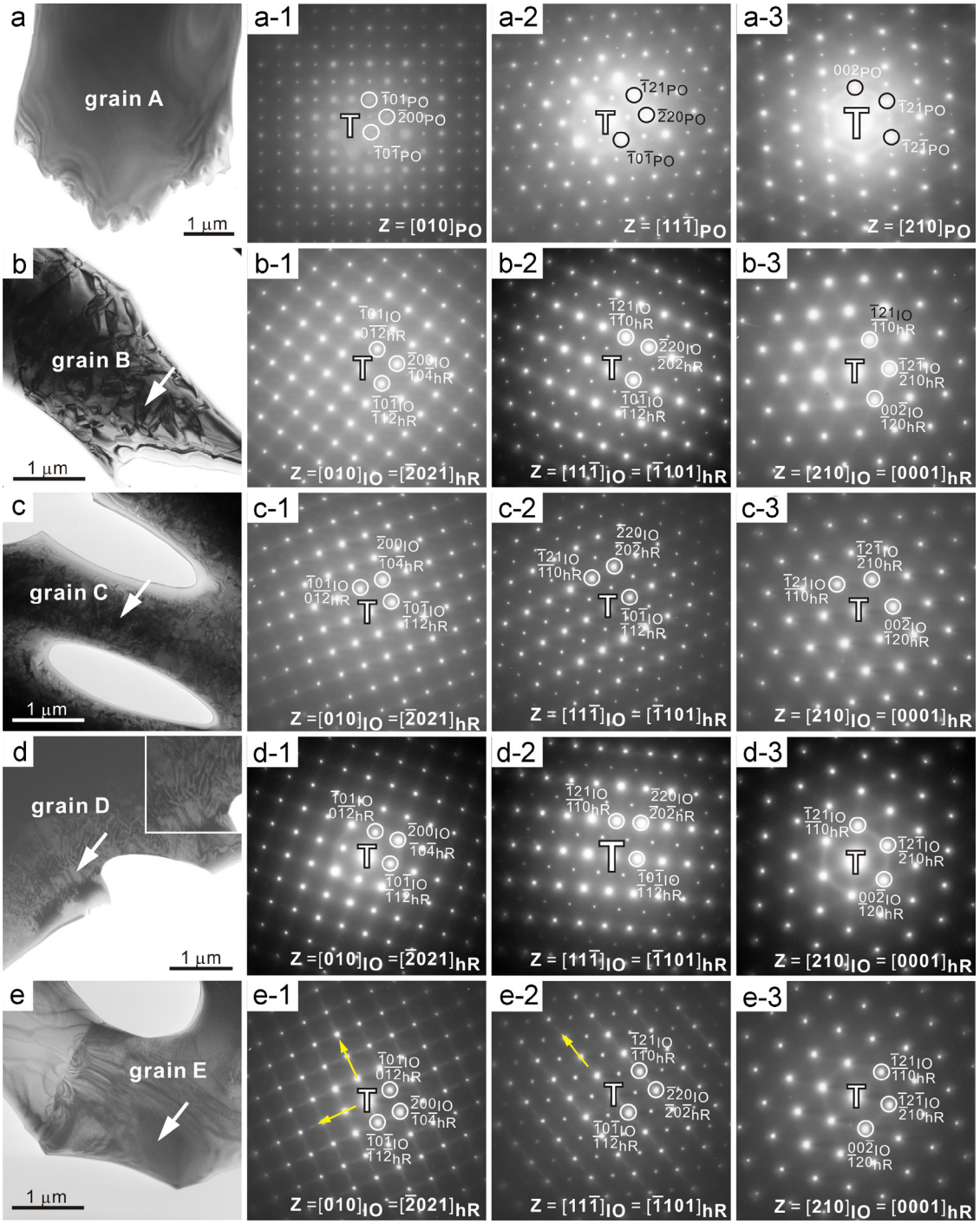

Fig. 4. TEM bright field images and SAED patterns of the LSGM samples sintered at 1500 °C for 10 h, (a) $LaGaO_3$, (b) LSGM1010, (c) LSGM1020, (d) LSGM1520, and (e) LSGM2020.

Doping with Sr and Mg ions is effective for producing oxygen vacancies, and their use further improves ionic conductivity. The data indicate that the crystal structures were altered by doping with aliovalent ions, as shown in Fig. 2(g) and (a)–(f), and the Raman-active vibrational modes decreased and broadened.

3.3. Microstructural analysis

The polished specimens were chemically etched, and the microstructures were observed by using SEM. Fig. 3 shows the SEM images of samples sintered at 1500 °C for 10 and 15 h. All specimens were quite dense, with relative densities of approximately 93–97%. Extremely sparse, small pores were present in the grain boundaries or trapped inside the grains.

A salient feature of the LSGM1010 and $LaGaO_3$ samples was observed [Fig. 3(a) and (g)]: the microstructures of these samples may be ascribed to twins, stacking faults, or antiphase phase boundaries induced by the phase transition. The microstructures could only be further analyzed using TEM. However, except for LSGM1010 and $LaGaO_3$, all other LSGM samples [Fig. 3(b)–(f-1)] did not display this salient feature, i.e., twins or stacking faults. The tilting of the GaO_6 octahedron decreased as the Sr and Mg contents increased beyond 0.3 mol; thus, the structure was closer to that of the more symmetrical systems, e.g., the hR phase. The average grain size (G_{av}) also increased significantly with increasing sintering time and amount of Sr and Mg, e.g., from 13 to 18 μm for sintering times of 10 to 15 h in the LSGM2015 sample and from 6.5 to 14.1 μm for $y=0.1$ to $y=0.2$ in the $La_{0.9}Sr_{0.1}Ga_{1-y}Mg_yO_{3-\delta}$ samples.

3.4. TEM analysis

Previous reports have shown that $La_{1-x}Sr_xGa_{1-y}Mg_yO_{3-\delta}$ ($x=0$–0.2, $y=0$–0.2) samples have five crystal structures that exist at different temperatures: PO-, IO-, M-, hR-, and C-phases [5–8]. The microstructures and phases of the LSGM samples were also analyzed by TEM. Fig. 4 shows the TEM bright field images (viewed from the zone axis $Z=[11\bar{1}]_{IO}$ or $[\bar{1}101]_{hR}$) and SAED patterns of the $LaGaO_3$, LSGM1010, LSGM1020, LSGM1520, and LSGM2020 samples. Defects were not clearly observed in grain A of $LaGaO_3$, and the patterns were indexed to $Z=[010]_{PO}$, $[11\bar{1}]_{PO}$, and $[210]_{PO}$ of the orthorhombic (*Pnma*) phase [Fig. 4(a)–(a-3)]. Stacking fault fringes were observed in the LSGM1010, LSGM1020, and LSGM1520 samples but not in the LSGM2020 sample. The fringes of stacking faults and defects decreased and gradually disappeared as the number of Mg and Sr ions increased, as shown by the arrows in Fig. 4(b)–(e). The stacking faults or defects were induced by the aggregation of oxygen vacancies. The patterns of the last four samples can be indexed to $Z=[010]_{IO}$ or $[\bar{2}021]_{hR}$, $[11\bar{1}]_{IO}$ or $[\bar{1}101]_{hR}$, and $[210]_{PO}$ or $[0001]_{hR}$ of the orthorhombic (*Imma*) or rhombohedral ($R\bar{3}c$) phases [Fig. 4(b)–(e-3)]. These patterns in the *Imma* phase are similar to those in the $R\bar{3}c$ phase from the simulated SAED patterns. The patterns are indexed to the IO-phase for LSGM1010 and LSGM1020 and to the hR-phase for LSGM1520 and LSGM2020 according to our previous XRD data. The tilting degree of octahedral GaO_6 decreased upon doping with Sr and Mg ions, which increased the structural symmetry [17,18].

3.5. Ionic conductivity

The conductivity was measured by the dc four-point probe method in air, which is a simple method for the determination of the total conductivity of a specimen. Fig. 5(a) shows the ionic conductivity of LSGM as a function of measuring temperature (500–800 °C). The conductivity depends strongly on the measuring temperature and dopant amount and increased significantly with increasing measuring temperature and increasing amounts of Sr and Mg. According to M. Shi et al. [19], higher

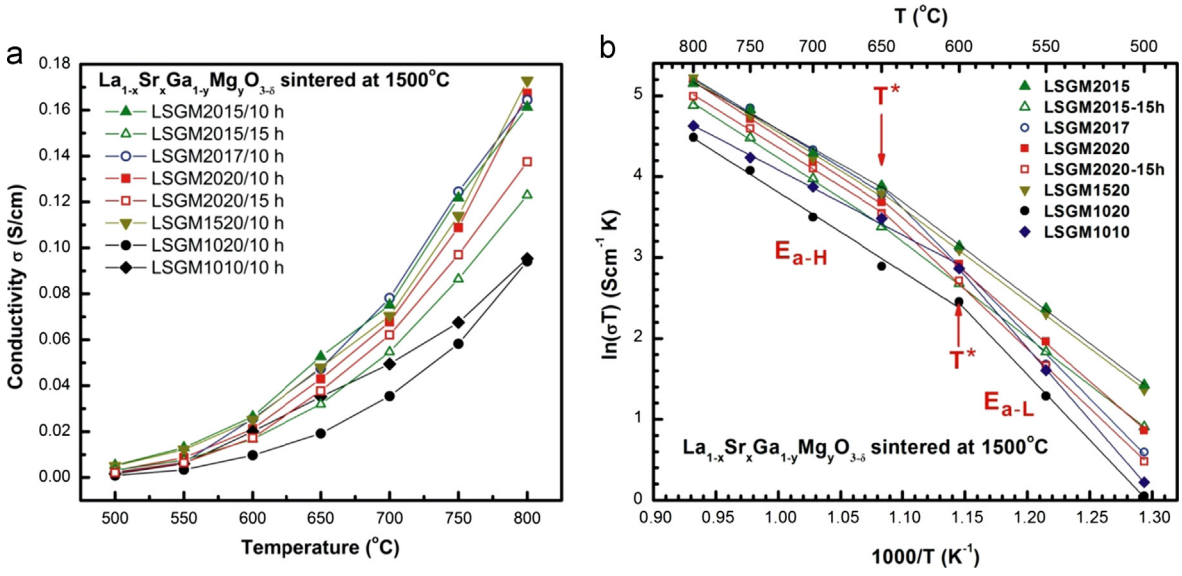

Fig. 5. DC conductivities of the LSGM samples sintered at 1500 °C for 10 and 15 h. (a) Temperature dependence of electrical conductivity and (b) Arrhenius plot of $\ln(\sigma T)$ and $1000/T$ (T^*: slope of the Arrhenius plot).

conductivity at higher measuring temperatures is the result of the acceleration of oxygen vacancy migration. The conductivities of LSGM1010, LSGM1520, and LSGM2020 were 0.095, 0.173, and 0.167 S/cm at 800 °C (Table 1 and Fig. 5), respectively, which is in good agreement with the values of 0.166 S/cm reported by Huang et al. [2] and 0.177 S/cm reported by Lu et al. [20] at 800 °C in the $La_{0.8}Sr_{0.2}Ga_{0.83}Mg_{0.17}O_{2.815}$ sample. When $x+y \geq 0.35$ mol, the conductivities of the samples were higher than 0.16 S/cm at 800 °C for a sintering period of 10 h (Table 1), and doping with Mg ions had a significant effect on increasing the ionic conductivity, i.e., $y=0.15$–0.20 at $x=0.2$.

In studying the effect of sintering time on conductivity, the conductivity clearly decreased from 0.167 to 0.137 S/cm with increasing sintering time from 10 to 15 h in the LSGM2020 specimens (similar to the LSGM2015 specimens) [Table 1, Figs. 5(a) and 6(a)]. When the Sr and Mg contents are fixed, a prolonged sintering time will increase the process of thermal activation, thereby promoting grain growth [Fig. 6(a)]. The larger grain size will increase the average pathways of oxygen ionic migration and thereby decrease the conductivity. However, it is obvious that the ionic conductivities of the LSGM ($x+y \geq 0.35$) samples in our study are higher than those of ZrO_2- or CeO_2-based oxides and somewhat lower than those of Bi_2O_3-based oxides [21]. The ionic conductivity can be expressed as

$$\sigma = \frac{\sigma_0}{T}\exp\left(\frac{-E_a}{kT}\right) \quad (2)$$

where σ, σ_0, T, E_a, and k are the ionic conductivity, pre-exponential factor, absolute temperature, activation energy, and Boltzmann constant (8.617343×10^{-5} eV/K), respectively. A plot of $\ln(\sigma T)$ vs. $1000/T$ should be a straight line with a slope equal to $-E_a/1000k$, allowing E_a to be calculated.

The Arrhenius plot of $\ln(\sigma T)$ and $1000/T$ is plotted in Fig. 5(b), and the slope changes dramatically at a T^* of approximately 600–650 °C. The change at T indicates a phase transformation or a change in the oxygen ionic conductive mechanism. Fig. 5(b) and Table 1 show that E_a is higher (0.99–1.54 eV) at low temperatures ($T < T^*$) and decreases (0.69–0.86 eV) with increasing temperature ($T > T^*$).

At $T < T^*$, the vacancies are progressively trapped into clusters to form ordered oxygen vacancies [2,17]. The oxygen migration pathways become longer as the oxygen atoms move through the clustered vacancies and the activation energy $E_{a\text{-}L}$ increases (as shown in Fig. 5(b)). At $T > T^*$, the vacancies are dissolved and distributed uniformly in the matrix. At this point, the pathways of the oxygen migration become shorter, and the activation energy $E_{a\text{-}H}$ decreases [2,17].

According to Skowron et al. [22], increasing the temperature destroys the planar ordering and eliminates the associated streaking on electron diffraction patterns in the LSGM2015 sample under high-temperature electron diffraction (20–900 °C) using TEM, with the electron diffraction patterns changing at approximately 500 °C [22]. This finding supports the claim that T^* in Fig. 5(b) is the temperature at which either a phase transformation or order–disorder oxygen vacancy transition occurred. The ionic conductivities at 800 °C, grain sizes, and activation energies of the LSGM samples are shown in Fig. 6.

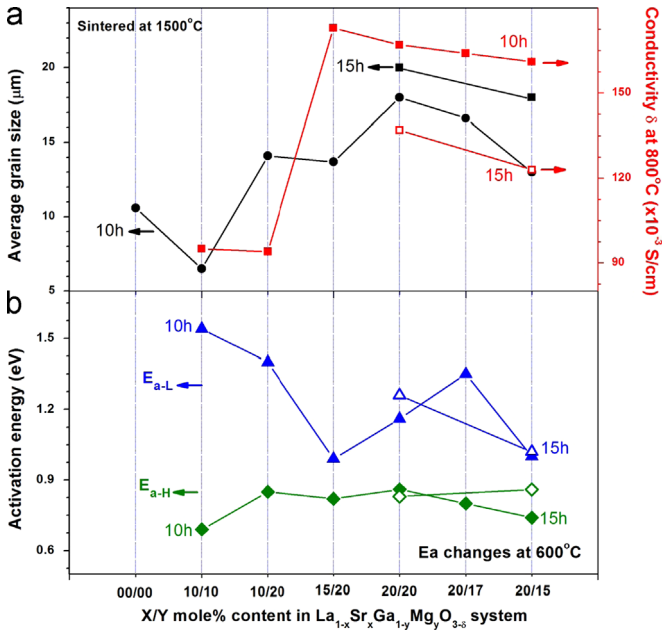

Fig. 6. Electrical conductivities at 800 °C, grain sizes, and activation energies as a function of LSGM composition.

Table 1
Electrical conductivities and activation energies of the LSGM ($x=0.1$–0.2, $y=0.1$–0.2) samples at 500–800 °C.

Specimen	Conductivity (S/cm) (10^{-3})							Activation energy (eV)		
	500 °C	550 °C	600 °C	650 °C	700 °C	750 °C	800 °C	$E_{a\text{-}L}$	T^* (°C)	$E_{a\text{-}H}$
LSGM2015-10 h	5	13	27	53	75	122	161	1.00	650	0.74
LSGM2017-10 h	2	7	26	47	78	125	164	1.35	650	0.80
LSGM2020-10 h	3	9	21	43	68	109	167	1.16	650	0.86
LSGM1520-10 h	5	12	25	48	70	114	173	0.99	650	0.82
LSGM1020-10 h	1	3	10	19	35	58	94	1.40	600	0.85
LSGM1010-10 h	1.6	6	20	35	49	68	95	1.54	600	0.69
LSGM2015-15 h	3	8	17	32	55	86	123	1.02	650	0.86
LSGM2020-15 h	2	6	17	38	62	97	137	1.26	650	0.83

3.6. AC impedance spectroscopy

Fig. 7 shows the ac (Nyquist) impedance spectra of the LSGM samples measured in the range 300–800 °C in air. Each semicircular arc corresponds to a series of resistance (R)–capacitor (C) combinations. The equivalent circuit mode assumes a total impedance that includes grain interior (R_{gi}), grain boundary (R_{gb}), and electrode polarization (R_e) effects. Because the LSGM specimens are not perfect, homogenous materials, a constant phase element (CPE) was added to the equivalent circuit mode instead of a capacitor. A CPE is needed when there is distortion introduced by local inhomogeneities, e.g., secondary phases, pores, local charge inhomogeneity, and variations in composition [23]. The equivalent circuit mode was designed to correspond to R_0-(R_{gi}/CPE_{gi})-(R_{gb}/CPE_{gb})-(R_e/CPE_e), where the hyphens (-) and slash marks (/) denote connections in series and in parallel, respectively, and R_0 is the unavoidable resistance associated with the testing equipment [24]. The high-frequency arc ($> 10^4$ Hz) represents the bulk response, the middle-frequency arc is the series grain boundary response according to the brick-layer model, and the low-frequency spike is the electrode response. The electrode response is more complicated because it is inclined at 45° from the vertical, called the Warburg response [25], because oxygen ions are unable to diffuse through the entire thickness of the electrode at the lowest frequency.

Fig. 7(A) and (B) shows two somewhat depressed arcs and one electrode spike at 300 °C and 400 °C, and feature a larger grain interior response and a small grain boundary response due to the larger grain size, respectively. These spectra were simulated using the Z-view software [26] for the equivalent circuit. For $T > 500$ °C, the impedance clearly decreases and is always below 200 Ω [Fig. 7(C)–(F)], and the conductivity values were approximately 4–7 Ω at 800 °C. The time constants ($\tau = RC$) of relaxation become very small [27], and the depressed semicircles of the grain interior and grain boundary therefore also become small and then disappear. The ac impedance spectra cannot be resolved because of the strong overlap of the grain interior and grain boundary semicircles. The electrode processes are dominant at 500 °C. Only one arc was

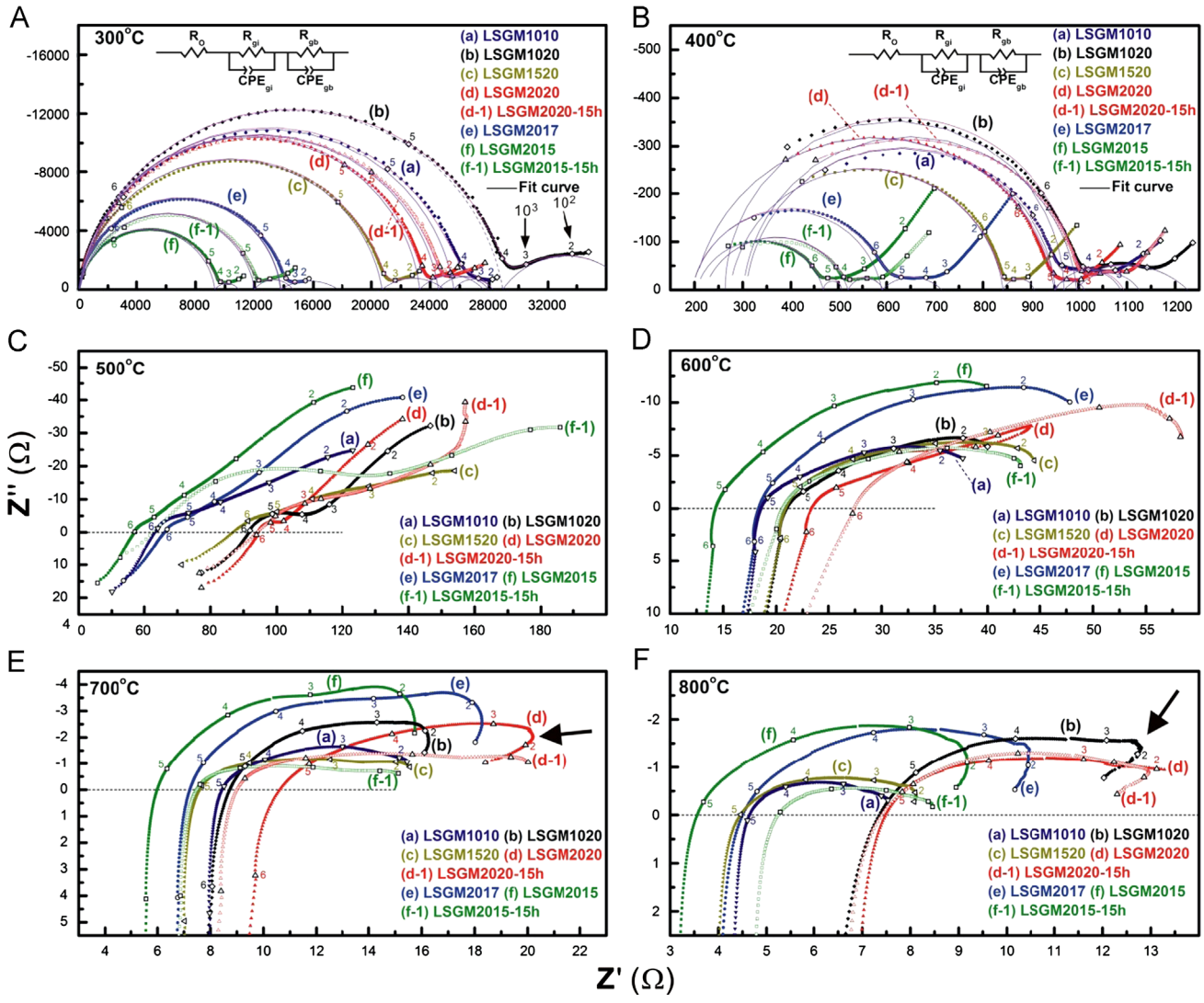

Fig. 7. AC impedance plots of the LSGM samples measured at 300–800 °C.

observed, and it shifted to higher frequencies above 500 °C as a result of strong electrode polarization processes [27].

The higher-frequency tails shown in Fig. 7(C) and (D) stem from the inductance (L) of the device and the connecting wiring [28,29]; the mode is designed as (R_0/L_{el})-(R_{gi}/CPE_{gi})-(R_{gb}/CPE_{gb})-(R_e/CPE_e). A similar phenomenon appeared in Fig. 7 (E) and (F) (700 and 800 °C), and the mode was corrected to R_0-L_{el}-(R_{gi}/CPE_{gi})-(R_{gb}/CPE_{gb})-(R_e/CPE_e) [28,30]. Reverse arcs appeared at a lower frequency at 700 and 800 °C [as indicated by arrows in Fig. 7(E) and (F), respectively] and are similar to the complex plane impedance of the active–passive transition of a metal–solution interface, as reported in the literature [31], and thus the reverse arc is attributed to the active electrode polarization interfacial processes.

The device and connecting wiring in the testing sample significantly influences the accuracy of the resistance measurements at higher temperatures. When the measuring temperature increases, variations in the impedance arc also increase. Only the ac impedance data at 300 °C and 400 °C were fitted to calculate the impedances and the capacitance of the grain interior and grain boundary using Eq. (3). The results are listed in Table 2.

$$C = R^{(1-n/n)}\ Q^{(1/n)} \tag{3}$$

where C, R, Q, and n are the capacitance, resistance, and the constant phase elements of CPE-T and CPE-P, respectively [32]. The CPE_{gi}-P of the bulk material was approximately 0.8–1, and it exhibited almost pure capacitance behavior. The CPE_{gb}-P of the grain boundary was approximately 0.36–1 (Table 2). The capacitances C_{gi} and C_{gb} were in the ranges of 23–99 pF and 26–753 nF, respectively, at 300–400 °C.

The total impedance varied significantly with the Sr and Mg contents at 300 and 400 °C, and the lower resistance occurred for x+y of approximately 0.35 [Figs. 7(A) and (B) and 8]. The LSGM1010 and LSGM1020 samples possessed higher resistances, and stacking faults and defects were present in the samples [Figs. 4(b) and (c) and 8]. At temperatures below 500 °C, these defects will cause oxygen ions to require higher energy to migrate.

For the LSGM2015, LSGM2017, and LSGM2020 samples, the resistance of the grain interior clearly increased with an increase in Mg content: $R_{gi\text{-}LSGM2015} < R_{gi\text{-}LSGM2017} < R_{gi\text{-}LSGM2020}$. However, the resistance of the grain boundary did not obviously change, which is also a result of the grain growth [Fig. 6(a)]. The energy barrier of the oxygen ions migrating along the grain interior is higher than that along the grain boundary at 300 and 400 °C, and the volume of the grain interior occupies a larger fraction of the sample than does the grain boundary. Thus, grain size is also the predominant characteristic for improved conductivity at 300–400 °C.

3.7. Thermal analysis

Fig. 9 shows the thermal expansion analyses of the LSGM1010, LSGM1020, LSGM1520, LSGM2020, and LSGM2015 samples from 25 °C to 800 °C. The thermal expansion coefficient is an important characteristic for the application of SOFCs. The physical

Table 2
AC impedance fitting results for the LSGM samples at 300 °C and 400 °C.

Sample	Temperature (°C)	R_0 (Ω)	R_{gi} (Ω)	CPE_{gi}-T (pF)	CPE_{gi}-P	C_{gi} (pF)	R_{gb} (Ω)	CPE_{gb}T (nF)	CPE_{gb}-P	C_{gb} (nF)	R_{gi}+R_{gb} (Ω)
LSGM1010-10 h	300	60	25,543	94	0.90	23	2633	1065	0.61	26	28,176
	400	307	646	170	0.94	65	135	3316	0.70	113	781
LSGM1020-10 h	300	25	28,895	107	0.90	24	8716	1774	0.61	128	37,611
	400	264	705	72	1	72	257	28,453	0.48	154	963
LSGM1520-10 h	300	25	20,701	108	0.90	25	4243	16,935	0.44	565	24,944
	400	273	568	243	0.92	64	67	6007	0.75	464	635
LSGM2015-10 h	300	72	9236	107	0.92	33	1634	2512	0.58	45	10,870
	400	204	265	1801	0.83	99	38	94	0.98	69	303
LSGM2017-10 h	300	67	13,710	84	0.93	32	3933	30,585	0.36	753	17,643
	400	195	395	561	0.89	81	125	30,000	0.50	113	520
LSGM2020-10 h	300	20	23,257	86	0.93	32	4435	7129	0.53	330	27,592
	400	200	750	280	0.90	46	62	5462	0.73	288	812
LSGM2015-15 h	300	77	12,110	124	0.90	26	1325	307	0.83	62	13,435
	400	220	300	2928	0.80	89	73	3331	0.75	199	373
LSGM2020-15 h	300	4	24,550	99	0.90	25	3408	3311	0.59	156	27,958
	400	301	694	148	0.95	61	130	10,903	0.63	226	824

expansion coefficient (α) is the slope of the relative length–change curve at a given temperature (T) [Eq. (4)], as shown in Fig. 9(B).

$$\alpha(T) = (1/l_0)(\mathrm{d}l/\mathrm{d}T)_p \quad (4)$$

where l_0 is the initial length of the sample. The TECs of the five samples range from 9.1×10^{-6}/°C to 11×10^{-6}/°C at 200–400 °C and from 10×10^{-6}/°C to 14×10^{-6}/°C at 500–800 °C, and a turning point appears at 475–550 °C [Fig. 9(B)]. The data show that the phase transition occurs at temperatures above approximately 500 °C, and the results are consistent with the slope change in the temperature range 600–650 °C, as shown in Fig. 5(b). This finding is also similar to those reported by Vasylechko et al. [6] and Shibasaki et al. [33]. Vasylechko et al. [6] reported that there are three phase transitions in LSGM0510, i.e., 247–297 °C (*Imma*–*I*2/*a*), 497 °C (*I*2/*a*–*R*3*c*), and 597 °C (*R*3*c*–*R*$\bar{3}$*c*), and two transitions in LSGM1020, i.e., 497 °C (*I*2/*a*–*R*3*c*) and 597–697 °C (*R*3*c*–*R*$\bar{3}$*c*).

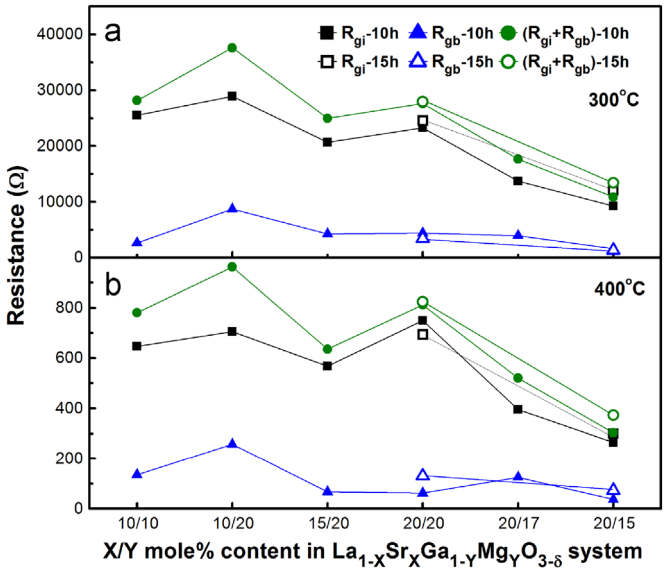

Fig. 8. Grain interior resistances, grain boundary resistances, and total resistances of the LSGM samples calculated from the ac impedance plots at 300 and 400 °C.

The differential thermal analysis (DTA) and thermogravimetric (TG) analysis results for the LSGM1010 and LSGM2020 samples are shown in Fig. 10. A sharp endothermic peak was detected at temperatures above 700 °C in the DTA curve, which is in agreement with the results reported by Chen et al. [34]. This finding verifies that gradual phase transitions occurred at ca. 700 °C. The obvious changes in weight varied with the change in temperature. The weight decreased with increasing temperature at 100–300 °C, and the decrease in weight was approximately 0.05%. This mass loss is due to the presence of absorbed water [35]. The weight then increased with increasing temperature beginning at approximately 300 °C, and the increase in weight was approximately 0.2% at 800 °C. When temperature decreased from 800 °C to room temperature, the weight returned to the total mass loss of 0.05%. Therefore, the variation of weight at 300–800 °C was due to the variation in the number of oxygen ions in the LSGM samples. The results verified that the ionic conductivity mechanism had changed or that gradual phase transitions occurred.

4. Conclusions

$La_{0.9}Sr_{0.1}Ga_{0.9}Mg_{0.1}O_{3-\delta}$ and $La_{0.9}Sr_{0.1}Ga_{0.8}Mg_{0.2}O_{3-\delta}$ samples are orthorhombic (*Imma*) in structure. $La_{1-x}Sr_xGa_{1-y}Mg_yO_{3-\delta}$ ($0.1 < x \leq 0.2$, $0.17 \leq y \leq 0.2$) samples with rhombohedral ($R\bar{3}c$) structure were obtained by sintering at 1500 °C for 10 h in a

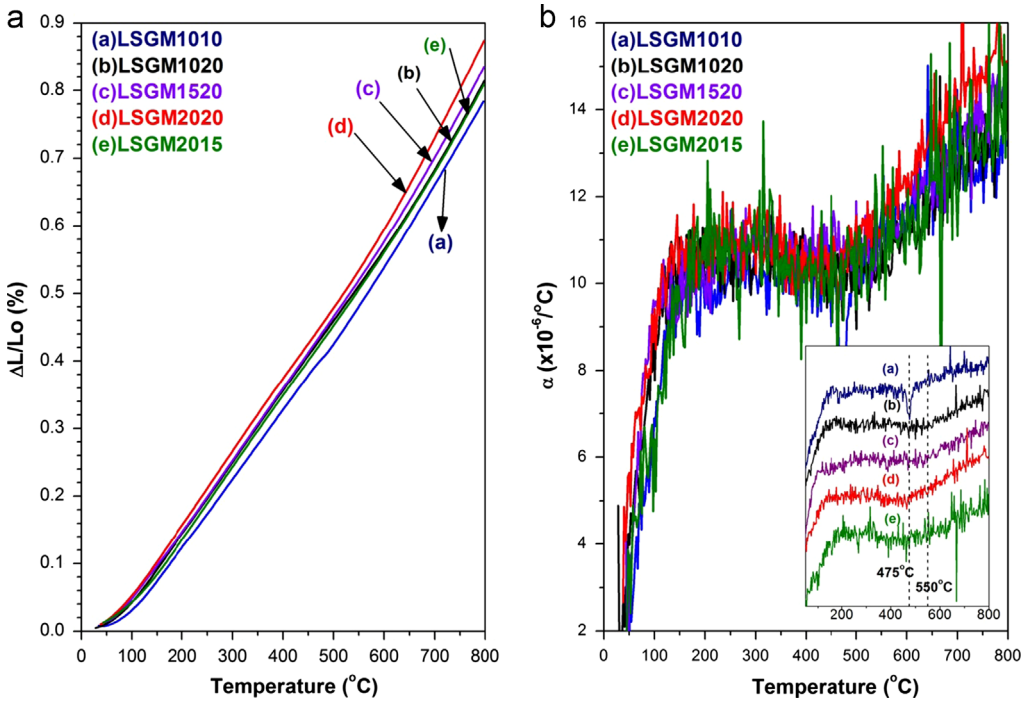

Fig. 9. Thermal expansion analyses of the (a) LSGM1010, (b) LSGM1020, (c) LSGM2020, and (d) LSGM2015 samples sintered at 1500 °C for 10 h.

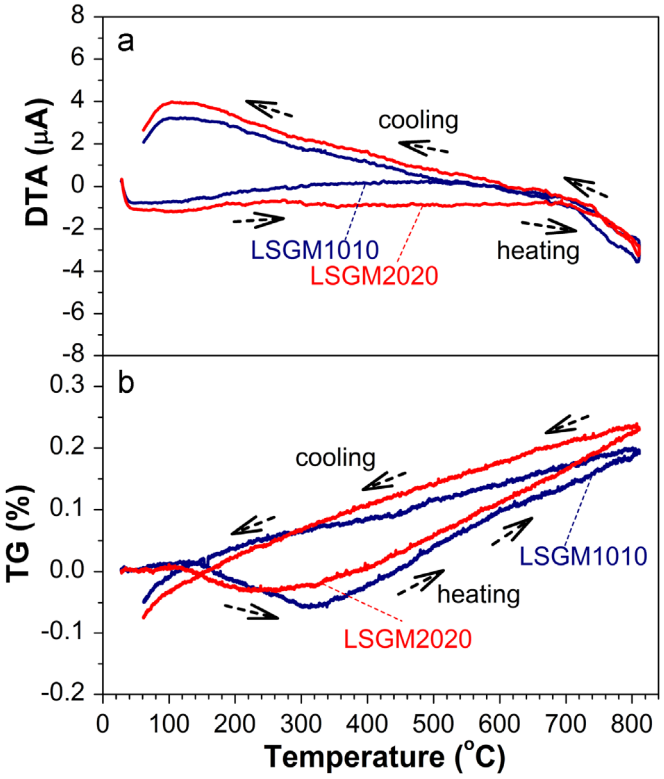

Fig. 10. (a) Differential thermal analysis and (b) thermogravimetric analysis of the LSGM1010 and LSGM2020 samples.

solid-state reaction. The average grain size increased with an increase in either the Sr and Mg contents or the sintering time. The relative densities of all LSGM samples were greater than 93%. $SrLaGa_3O_7$ was observed as a result of excess Sr in the LSGM sample. Active bands at approximately 532, 674, and 750 cm^{-1} appeared as a result of a decrease in the local symmetry induced by the oxygen vacancies.

The conductivity clearly increased as a result of an increase in either the measuring temperature or the amount of Sr and Mg and decreased with an increase in grain size. When the amount of co-doping of Sr and Mg exceeds 0.35 mol, the conductivity is approximately 0.164–0.173 S/cm at 800 °C. A phase transformation occurred or the oxygen ionic conductive mechanism changed at a T^* of approximately 500–650 °C. The LSGM1010 and LSGM1020 samples possessed larger resistances for grain interiors and grain boundaries at 300–400 °C as a result of existing stacking faults and defects. Stacking faults gradually decreased with an increase in dopant content. The TECs of the LSGM sample were approximately 9.1×10^{-6}/°C to 14×10^{-6}/°C at 200–800 °C.

Acknowledgments

We thank the National Science Council of Taiwan for the funding support through Contracts NSC 99-2221-E-027-082, NSC 100-2221-E-027-109, and NSC 101-2221-E-027-021.

References

[1] P. Huang, A. Petric, Superior oxygen ion conductivity of lanthanum gallate doped with strontium and magnesium, Journal of the Electrochemical Society 143 (1996) 1644–1648.
[2] K. Huang, R.S. Tichy, J.B. Goodenough, Superior perovskite oxide-ion conductor; strontium- and magnesium-doped $LaGaO_3$: I. Phase relationships and electrical properties, Journal of the American Ceramic Society 81 (1998) 2565–2575.
[3] Y. Wang, X. Liu, G.D. Yao, R.C. Liebermann, M. Dudley, High temperature transmission electron microscopy and X-ray diffraction studies of twinning and the phase transition at 145 °C in $LaGaO_3$, Materials Science and Engineering A 132 (1991) 13–21.
[4] I.A. Leonidov, I.V. Baklanova, L.A. Perelyaeva, O.N. Leonidova, R.F. Samigullina, V.L. Kozhevnikov, The effect of divalent cations on the structural parameters, phase transitions, and electrical conductivity of oxygen conductors based on $LaGaO_3$, Doklady Chemistry 427 (2009) 194–198.
[5] P.R. Slater, J.T.S. Irvine, T. Ishihara, Y. Takita, High-temperature powder neutron diffraction study of the oxide ion conductor $La_{0.9}Sr_{0.1}Ga_{0.8}Mg_{0.2}O_{2.85}$, Journal of Solid State Chemistry 139 (1998) 135–143.
[6] L. Vasylechko, V. Vashook, D. Savytskii, A. Senyshyn, R. Niewa, M. Knapp, H. Ullmann, M. Berkowski, A. Matkovskii, U. Bismayerg, Crystal structure, thermal expansion and conductivity of anisotropic $La_{1-x}Sr_xGa_{1-2x}Mg_{2x}O_{3-y}$ (x=0.05, 0.1) single crystals, Journal of Solid State Chemistry 172 (2003) 396–411.
[7] M.M. Guenter, M. Lerch, H. Boysen, D. Toebbens, E. Suard, C. Baehtz, Combined neutron and synchrotron X-ray diffraction study of Sr/Mg-doped lanthanum gallates up to high temperatures, Journal of Physics and Chemistry of Solids 67 (2006) 1754–1768.
[8] M. Kajitani, M. Matsuda, A. Hoshikawa, S. Harjo, T. Kamiyama, T. Ishigaki, F. Izumi, M. Miyake, Doping effect on crystal structure and conduction property of fast oxide ion conductor $LaGaO_3$-based perovskite, Journal of Physics and Chemistry of Solids 68 (2007) 758–764.
[9] D. Marrero-López, M.C. Martín-Sedeño, J. Peña-Nartínez, J.C. Ruiz-Morales, P. Núñez-Coello, J.R. Ramos-Barrado, Microstructure and conductivity of $La_{1-x}Sr_xGa_{0.8}Mg_{0.2}O_{3-\delta}$ electrolytes prepared using the freeze-drying method, Journal of the American Ceramic Society 94 (2011) 1031–1039.
[10] S. Li, B. Bergman, Doping effect on secondary phases, microstructure and electrical conductivities of $LaGaO_3$ based perovskites, Journal of the European Ceramic Society 29 (2009) 1139–1146.
[11] V.V. Kharton, A.L. Shaula, N.P. Vyshatko, F.M.B. Marques, Electron–hole transport in $(La_{0.9}Sr_{0.1})_{0.98}Ga_{0.8}Mg_{0.2}O_{3-\delta}$ electrolyte: effects of ceramic microstructure, Electrochimica Acta 48 (2003) 1817–1828.
[12] K. Huang, R.S. Tichy, J.B. Goodenough, C. Milliken, Superior perovskite oxide-ion conductor; strontium- and magnesium-doped $LaGaO_3$: III. Performance tests of single ceramic full cells, Journal of the American Ceramic Society 81 (1998) 2581–2585.
[13] K.T. Jacob, S. Jain, V.S. Saji, P.V.K. Spikanth, Thermal expansion of doped lanthanum gallates, Bulletin of Materials Science 33 (2010) 407–411.
[14] P. Datta, P. Majewski, F. Aldinger, Thermal expansion behaviour of Sr- and Mg-doped $LaGaO_3$ solid electrolyte, Journal of the European Ceramic Society 29 (2009) 1463–1468.
[15] G.A. Tompsett, N.M. Sammes, R.J. Phillips, Raman spectroscopy of the $LaGaO_3$ phase transition, Journal of Raman Spectroscopy 30 (1999) 497–500.
[16] T. Inagaki, K. Miura, H. Yoshida, J. Fujita, M. Nishimura, Raman studies of $LaGaO_3$ and doped $LaGaO_3$, Solid State Ionics 118 (1999) 265–269.
[17] J.A. Kilner, R.J. Brook, A study of oxygen ion conductivity in doped non-stoichiometric oxides, Solid State Ionics 6 (1982) 237–252.
[18] R.A.D Souza, M. Martin, An atomistic simulation study of oxygen-vacancy migration in perovskite electrolytes based on $LaGaO_3$, Monatshefte für Chemie/Chemical Monthly 140 (2009) 1011–1015.

[19] M. Shi, N. Liu, Y. Xu, Y. Yuan, P. Majewski, F. Aldinger, Synthesis and characterization of Sr- and Mg-doped $LaGaO_3$ by using glycine–nitrate combustion method, Journal of Alloys and Compounds 425 (2006) 348–352.

[20] X.C. Lu, J.H. Zhu, Effect of Sr and Mg doping on the property and performance of the $La_{1-x}Sr_xGa_{1-y}Mg_yO_{3-\delta}$ electrolyte, Journal of the Electrochemical Society 155 (2008) 494–503.

[21] T. Ishihara, Development of new fast oxide ion conductor and application for intermediate temperature solid oxide fuel cells, Bulletin of the Chemical Society of Japan 79 (2006) 1155–1166.

[22] A. Skowron, P. Huang, A. Petric, Structural study of $La_{0.8}Sr_{0.2}$-$Ga_{0.85}Mg_{0.15}O_{2.825}$, Journal of Solid State Chemistry 143 (1999) 202–209.

[23] S. Li, Z. Li, B. Bergman, Lanthanum gallate and ceria composite as electrolyte for solid oxide fuel cells, Journal of Alloys and Compounds 492 (2010) 392–395.

[24] P. Fang, S.P. Li, J.Q. Lu, Z.Y. Pu, S.Q. Cen, M.F. Luo, Effect of phase structure on electrical conductivity of $Ce_xGd_{1-x}O_{2-\delta}$ solid electrolytes, Materials Science and Engineering B 164 (2009) 101–105.

[25] E.J. Abran, D.C. Sinclair, A.R. West, Electrode-contact spreading resistance phenomena in doped-lanthanum gallate ceramics, Journal of Electroceramics 7 (2001) 179–188.

[26] D. Johnson, ZView2: A Software Program for IES Analysis, Version 3.0, Scribner Associates Inc., Southern Pines NC, 2007.

[27] M.G. Chourashiya, J.Y. Patil, S.H. Pawar, L.D. Jadhav, Studies on structural, morphological and electrical properties of $Ce_{1-x}Gd_xO_{2-(x/2)}$, Materials Chemistry and Physics 109 (2008) 39–44.

[28] A. Bieberle-Hütter, M. Søgaard, H.L. Tuller, Electrical and electrochemical characterization of microstructured thin film $La_{1-x}Sr_xCoO_3$ electrodes, Solid State Ionics 177 (2006) 1969–1975.

[29] M.J. Escudero, A. Aguadero, J.A. Alonso, L. Daza, A kinetic study of oxygen reduction reaction on La_2NiO_4 cathodes by means of impedance spectroscopy, Journal of Electroanalytical Chemistry 611 (2007) 107–116.

[30] D. Chen, R. Ran, K. Zhang, J. Wang, Z. Shao, Intermediate-temperature electrochemical performance of a polycrystalline $PrBaCo_2O_{5+\delta}$ cathode on samarium-doped ceria electrolyte, Journal of Power Sources 188 (2009) 96–105.

[31] E. Barsoukov, J.R. Macdonald, in: Impedance Spectroscopy: Theory, Experiment, and Applications, 2nd ed., John Wiley & Sons Inc., Hoboken New Jersey, 2005, pp. 363–368.

[32] Q. Li, V. Thangadurai, Synthesis, structure and electrical properties of Mo-doped CeO_2-materials for SOFCs, Fuel Cells 9 (2009) 684–698.

[33] T. Shibasaki, T. Furuya, S. Wang, T. Hashimoto, Crystal structure and phase transition behavior of $La_{1-x}Sr_xGa_{1-y}Mg_yO_{3-\delta}$, Solid State Ionics 174 (2004) 193–203.

[34] T.Y. Chen, K.Z. Fung, Synthesis of and densification of oxygen-conducting $La_{0.8}Sr_{0.2}Ga_{0.8}Mg_{0.2}O_{2.8}$ nano powder prepared from a low temperature hydrothermal urea precipitation process, Journal of the European Ceramic Society 28 (2008) 803–810.

[35] P. Datta, P. Majewski, F. Aldinger, Synthesis and microstructural characterization of Sr- and Mg-substituted $LaGaO_3$ solid electrolyte, Materials Chemistry and Physics 102 (2007) 240–244.